Photoluminescence Probes Ion Insertion into Amorphous and Crystalline Regions of Organic Mixed Conductors

Garrett W. Collins, Mohd Sajid Lone, Seth R. Jackson, Jolene N. Keller, Rand L. Kingsford, Rodrigo Noriega, Connor G. Bischak*

Department of Chemistry, University of Utah, Salt Lake City, UT 84112, United States

KEYWORDS. Conjugated polymers, organic mixed conductors, photoluminescence, in situ methods, electrochemical doping

Abstract: Organic mixed ionic-electronic conductors (OMIECs) have emerged as promising materials for a wide range of next-generation technologies, including bioelectronics and neuromorphic computing. The performance of these materials depends on the transport of ions through the polycrystalline polymer matrix as well as how the distribution of ions and polarons in crystalline and amorphous regions impacts electronic transport. However, it is often challenging to distinguish whether ions enter crystalline or amorphous regions. In this work, we use steady-state and time-resolved photoluminescence (PL) spectroelectrochemistry to probe initial ion insertion in crystalline and amorphous regions of the OMIEC material poly(3-[2-[2-(2-methoxyethoxy)ethoxy]ethyl]thiophene -2,5-diyl) (P3MEEET) as a function of applied voltage. We find that PL spectroelectrochemistry reports on the initial stages of electrochemical doping through the quenching of PL emission. By distinguishing between amorphous and crystalline contributions to the PL spectrum, we track ion insertion in crystalline and amorphous regions as a function of voltage. We find that PL spectroelectrochemistry is much more sensitive to the initial injection of ions than complementary methods, highlighting its potential as a sensitive tool for interrogating ion injection in OMIECs.

1. INTRODUCTION

Organic mixed ionic-electronic conductors (OMIECs) are typically semiconducting polymers with conjugated backbones that facilitate electron transport and side chains that promote ion mobility.[1] This family of materials has drawn considerable interest for applications that leverage mixed conduction, including bioelectronics,[2,3] biosensors,[4] neuromorphic computing,[5–7] and energy storage.[8,9] These technologies rely on electrochemical doping, in which electronic charge carriers are injected into the OMIEC from an underlying electrode, and ions from the adjacent electrolyte enter the polymer matrix to achieve charge neutrality, forming ion-polaron pairs. Electrochemical doping is reversible, as reversing the applied bias can return the OMIEC to its neutral state.

Because OMIECs operate in a liquid environment, traditional techniques established to probe structural, electronic, and chemical properties of unhydrated conjugated polymer thin films are insufficient for studying structure-property relationships in OMIECs. Therefore, developing new methods that probe OMIECs in a liquid electrolyte is critical to elucidating OMIEC operation and developing new design principles for more efficient devices.[10,11] Wu et al. summarized *operando* methods for probing OMIECs in a recent review article.[10] These methods include optical spectroelectrochemistry,[12–15] X-ray and neutron scattering,[16,17] electrochemical quartz crystal microbalance (EQCM),[18] magnetic resonance spectroscopies,[19,20] and various scanning probe imaging methods.[21–24] Although numerous methods exist to probe OMIECs *in situ*, these methods can be challenging to implement and often require custom *in situ* sample cells. Additionally, many of these methods are not sensitive to the initial insertion of ions and cannot distinguish between doping in amorphous versus crystalline regions.

Of the *operando* methods used to interrogate OMIECs, UV-Vis absorption spectroelectrochemistry is one of the most widely used. In its neutral state, the absorption spectrum of p-type OMIECs typically features a single absorption peak from the π-π* electronic

transition. The intensity of the π-π* peak decreases upon electrochemical doping, and new redshifted absorption peaks appear due to polaron and bipolaron formation.[12,25,26] Other *operando* spectroelectrochemistry approaches, such as Raman spectroscopy,[13,27–29] transient absorption spectroscopy,[14,30–32] and terahertz (THz) spectroscopy[15] have been used to interrogate ion injection in OMIECs. The structural, chemical, and spectral resolution of these tools has been crucial to fundamental studies of doping processes in OMIECs; however, these techniques respond to changes in the material due to the inclusion of a large number of ions. To understand the earliest stages of doping, it is necessary to employ a probe that is highly responsive, with a low background and a robust output that encodes structurally-specific signatures; moreover, for its widespread application, a simple and low-cost instrument would be desirable. The strong dependence of charge transport on the microstructure of polymer films has long been established in traditional conjugated polymer applications;[33,34] however, the optimal balance between ordered and disordered components in OMIECs is a matter of debate. Thus, a simple technique capable of detecting early doping in a structurally-sensitive manner would prove useful to the field and expand the reach of operando structure-property studies.

Photoluminescence (PL) spectroelectrochemistry is a promising approach to probe the initial stages of ion injection in OMIECs and differentiate between doping in amorphous versus crystalline regions. Previous investigations of the PL emission of conjugated polymers show that dopants serve as trap sites for photogenerated excitons and suppress radiative recombination.[35,36] Because excitons migrate within the polymer matrix, a single dopant can quench exciton emission from a large area.[37] For instance, in polythiophene films doped with 0.06 ClO_4^- per monomer, Hayashi et al. showed that the π-π* absorption peak intensity decreases by only 15%. In comparison, the PL intensity decreases by a much larger amount (i.e. 95% compared to that of an undoped film),[38] indicating the sensitivity of PL emission to low dopant densities. PL spectroscopy has also been used to characterize organic field effect transistors

(OFETs)[35] and light-emitting electrochemical cells (LECs).[39,40] Holt et al. studied changes in the PL of poly[2-methoxy-5-(2-ethylhexyloxy)-1,4-phenylenevinylene] (MEH-PPV) and determined that the PL was fully quenched 0.15 V before any color changes occurred within the polymer. They attributed the sensitivity of PL spectra to the ability of a single dopant to quench an entire polymer chain.[41] PL quenching has also been utilized to visualize and quantify the electrochemical doping front of p-type and n-type doping in LECs.[42,43] In addition to steady-state PL measurements, time-resolved PL (TRPL) has been used to understand how crystallinity impacts the exciton lifetime of conjugated polymers.[44,45] Compared to crystalline regions, amorphous regions have a shorter exciton diffusion length and an increased exciton lifetime. Another advantage of PL spectroscopy is its ability to distinguish between emission from amorphous and crystalline regions of conjugated polymer thin films. Spano et al. showed that aggregated and unaggregated regions of poly(3-hexylthiophene) (P3HT) exhibit different absorption and PL spectral signatures.[46,47]

One significant challenge to developing efficient OMIEC-based devices is determining where the ions and polarons reside. Although many previous studies have investigated the location of ions and polarons in OMIEC materials, a consensus has yet to emerge. For example, separate studies using different approaches have independently concluded that ions enter amorphous regions of conjugated polymers,[22] polarons reside in crystalline regions and ions initially reside in the boundary between amorphous and crystalline regions,[48] and that ions and polarons are colocalized in crystalline regions.[15,49] Determining the location of electronic and ionic species in OMIECs and how the arrangement of these species impacts charge transport remains a challenge that requires the development of new *in situ* methods.

Here, we establish steady-state PL and TRPL spectroelectrochemistry as methods to probe electrochemical doping and dedoping in crystalline and amorphous regions of OMIECs. We focus on poly(3-[2-(2-[2-methoxyethoxy]ethoxy)ethyl]thiophene-2,5-diyl) (P3MEEET), a conjugated

polymer OMIEC with a thiophene backbone and oligioglycol side chains that has emerged as a prototypical OMIEC material that exhibits relatively high performance when incorporated in an organic electrochemical transistor (OECT).[50,51] By acquiring PL spectra of P3MEEET as a function of voltage and decomposing the PL spectra into contributions from the amorphous and crystalline regions, we find that crystalline regions of the polymer are doped first, followed by the amorphous regions. We also find that PL lifetime is altered at higher doping levels than those required to observe a response in PL intensity. Furthermore, we compare PL emission intensity versus applied voltage with established *in situ* methods that probe ion intercalation in OMIECs. We find that PL intensity is significantly more sensitive to the very initial injection of ions than these established methods. Last, we show that PL spectroelectrochemistry reports on irreversible changes in OMIEC materials upon repeated electrochemical cycling that are not detected by absorption spectroelectrochemistry. Overall, we establish steady-state PL and TRPL spectroelectrochemistry as methods that are highly sensitive to the initial steps of electrochemical doping and that can distinguish between doping in amorphous and crystalline regions.

1. RESULTS AND DISCUSSION

Figure 1A shows a cyclic voltammogram (CV) of a P3MEEET thin film on an indium tin oxide (ITO) coated glass substrate in 100 mM KCl. The inset shows the chemical structure of P3MEEET, which has a polythiophene backbone and oligoglycol side chains. The CV shows that the oxidation or electrochemical doping onset of P3MEEET occurs around 0.1 V followed by an increase in the current. The oxidation of P3MEEET is reversible, as the CV also shows the subsequent reduction or electrochemical dedoping upon decreasing the voltage. **Figure 1B** depicts the normalized absorption and PL spectra of a P3MEEET thin film. In both the absorption and PL emission spectra, we observe clear vibronic peaks, indicating that P3MEEET thin films have a high degree of crystalline content. We confirm the polycrystallinity of P3MEEET by acquiring a GIWAXS pattern (**Figure S1**), which shows the characteristic lamellar and π-π stacking peaks typical of

polythiophenes.[52] We note that we observe both a disordered π-π stacking peak reminiscent of regiorandom poly(3-hexylthiophene) (P3HT) and an ordered π-π stacking peak similar to that of regioregular P3HT.[53,54] We also use atomic force microscopy (AFM) to confirm that the spin coated P3MEEET thin films are uniform with a surface roughness of 1.2 nm (**Figure S2**) and a thickness of 64 ± 7 nm.

To benchmark the PL spectroelectrochemistry to a more established method, we initially perform UV-Vis spectroelectrochemistry. We perform 10 CVs (-0.2 V to 0.6 V at 0.1 V/s) to acclimate the polymer to the aqueous electrolyte, and we then collect absorption spectra of P3MEEET as a function of voltage in 100 mM KCl. For the absorption spectra, we initially observe a π-π* absorption peak centered at 510 nm that decreases in intensity as we increase the voltage from -0.2 V to 0.6 V in 0.04 V steps (**Figure 1C**). As the π-π* peak decreases in intensity, a new redshifted peak centered at 750 nm emerges that corresponds to the formation of polarons in the P3MEEET matrix. As we decrease the voltage, electrochemical dedoping occurs and we observe a decrease in the absorption intensity of the polaron peak back to the baseline and an increase in the absorption intensity of the π-π* back to its original intensity (**Figure 1D**).

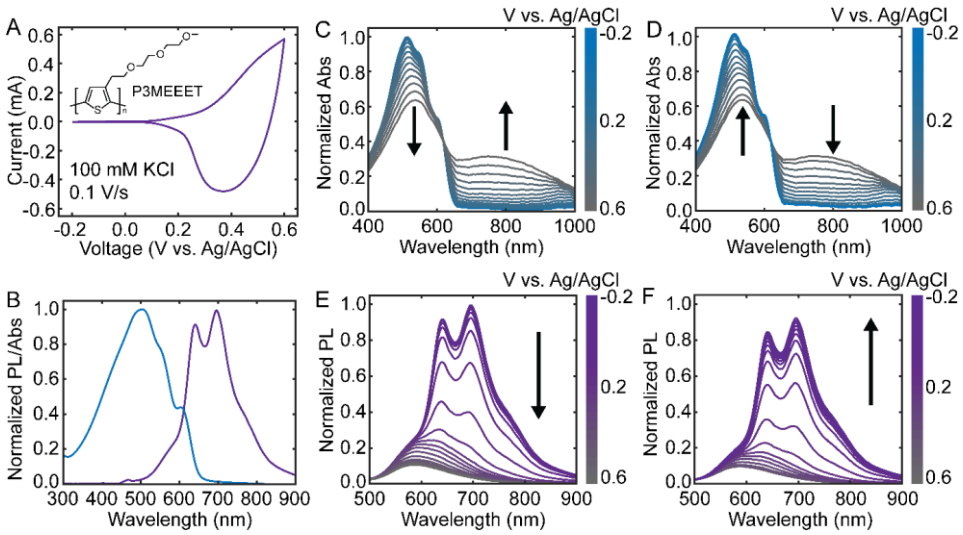

Figure 1. Electrochemical, optical, and spectroelectrochemical properties of P3MEEET in 100 mM KCl. A) Cyclic voltammograms (CVs) of a P3MEEET thin film with an inset showing the molecular structure of P3MEEET. B) Absorption (blue) and PL (purple) spectra of a P3MEEET thin film. Absorption spectra as a function of voltage during

C) electrochemical doping and D) dedoping normalized to the undoped absorption spectrum. PL spectra as a function of voltage during E) electrochemical doping and F) dedoping normalized to the initial undoped PL spectrum.

We next measure PL emission spectra as a function of voltage upon electrochemical doping 0-experimental setup. **Figure 1E** shows PL emission spectra as a function of increasing voltage under the same conditions as the absorption spectra displayed in **Figure 1C** (-0.2 V to 0.6 V in 0.04 V steps). As we increase the voltage, the PL emission spectrum decreases in intensity, indicating quenching of photogenerated excitons in P3MEEET, as observed previously in conjugated polymers upon doping.[35,36,38,41] Upon decreasing the applied voltage and dedoping the P3MEEET thin film (**Figure 1F**), we observe a recovery of the PL emission peak. Unlike the full recovery of the absorption spectrum upon doping and dedoping, the PL spectrum acquired after cycling returns to approximately 90% of its initial intensity. We conclude that this slight irreversibility of the PL intensity is due to either irreversible changes in the polymer morphology or irreversible quenching due to trapped ions in the film upon doping and dedoping rather than photobleaching, as PL spectra taken before and after an experiment where no other light was shone on the sample does not show a significant decrease in the PL emission intensity (**Figure S4**).

To separate the PL spectrum into its amorphous and crystalline components, we fit each PL spectrum using a method first described by Spano et al.[46,47] We fit the disordered component of the PL spectrum to a single Gaussian and we fit the crystalline component of the PL emission to a normalized Franck-Condon progression. **Figure 2A-D** shows examples of these fits at different doping levels. To achieve these fits, the unaggregated or disordered component was modeled as a simple Gaussian (**Equation 1**):

$$G(h\nu) = e^{-\frac{(h\nu - E_a)^2}{2{S_a}^2}} \quad (1)$$

where $G(h\nu)$ is the PL emission from amorphous regions of the polymer film, $h\nu$ is the photon energy in eV, E_a is the center wavelength of the Gaussian in eV, and S_a is the Gaussian width in

eV. We note that the spectral component that we assign to the disordered region closely matches the PL spectrum of P3MEEET dissolved in chloroform (0.01 mg/mL) (**Figure S5**). The PL emission that corresponds to the crystalline regions was modeled by a normalized Franck-Condon progression (**Equation 2**):

$$FC(h\nu) = \sum_{n=0}^{6} \frac{e^{-S}S^{n}}{n!} \cdot \frac{e^{-\frac{(h\nu - E_0 - nE_p)^2}{2\sigma^2}}}{\sigma} \quad (2)$$

where $FC(h\nu)$ is the PL emission for crystalline regions of the polymer film, *S* is the Huang-Rhys factor, *σ* is the width in eV of each transition, E_o is the vertical transition line, and E_p is the phonon energy. Summing together **Equation 1** and **Equation 2** gives a model of the PL spectra at all doping levels (**Equation 3**):

$$I(h\nu) = a \cdot G(h\nu) + c \cdot FC(h\nu) \quad (3)$$

where $I(h\nu)$ is the total PL intensity, $h\nu$ is the photon energy in eV, *c* is a coefficient representing the contribution of PL from the crystalline regions, and *a* is a coefficient representing the contribution of PL from the amorphous regions. We employ a least-squares regression to determine the best fits using **Equation 3**. By using this fit, we decompose the contributions to the PL emission spectra at each voltage into its amorphous and crystalline contributions. **Figure 2E** shows the integrated PL from crystalline regions and **Figure 2F** shows the integrated PL emission from amorphous regions as a function of voltage.

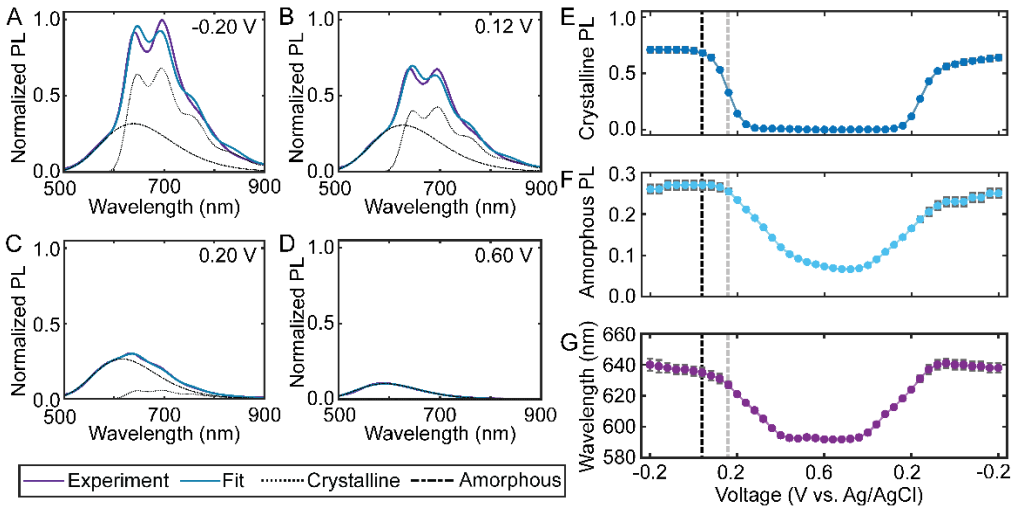

Figure 2. Voltage-dependent PL spectra and decomposition into crystalline and amorphous components. A-D) Overlays of the acquired PL spectra and fits of the PL spectra at different voltages using the sum of a single Gaussian fit for the PL from amorphous regions and a Franck-Condon progression for the PL from crystalline domains. E) PL emission from crystalline regions of P3MEEET as a function of voltage vs. Ag/AgCl. F) PL emission from amorphous regions of P3MEEET as a function of voltage vs. Ag/AgCl. G) Peak wavelength of the PL from amorphous regions of P3MEEET as a function of voltage vs. Ag/AgCl. The black and gray dotted lines correspond to the onset of PL quenching from crystalline and amorphous regions, respectively.

By decomposing the PL emission contributions of the crystalline and amorphous regions of the OMIEC, we observe that the most crystalline regions dope first followed by the amorphous regions. This is presumably due to the lower oxidation onset or more shallow HOMO level of the crystalline regions, which is consistent with prior studies.[15,48] We indicate the onset of quenching of crystalline and amorphous regions in **Figure 2** with black and gray dotted lines, respectively. We additionally track the maximum of the Gaussian fit of the amorphous PL emission as a function of voltage to determine how the amorphous regions of P3MEEET dope (**Figure 2G**). We find that the peak wavelength shifts from ~640 nm to ~590 nm and then plateaus as we increase the voltage. We interpret this shift in the peak PL emission wavelength as doping amorphous regions with progressively deep HOMO levels. The plateau in the wavelength versus voltage as well as the amorphous PL intensity versus voltage at higher doping potentials indicates that some regions with relatively low HOMO levels are not capable of doping perhaps due to the low electron mobilities of these regions.

We also use TRPL to probe the photoluminescence decay of the crystalline and amorphous regions of P3MEEET. Here, we used a 530 nm excitation source to excite the crystalline regions of the polymer and a 400 nm excitation source to excite both crystalline and amorphous regions of the P3MEEET film. Examples of TRPL traces using the 530 nm and 400 nm excitation wavelengths are depicted in **Figure 3A** and **Figure 3B**, respectively. A background PL decay curve was also collected from the ITO with no P3MEEET coating, the cuvette, and the 100 mM KCl aqueous electrolyte solution. The background was collected with an integration time of 1200 seconds for the 530 nm excitation and 1000 seconds for the 400 nm excitation, which was subtracted from the acquired TRPL traces of the P3MEEET thin films.

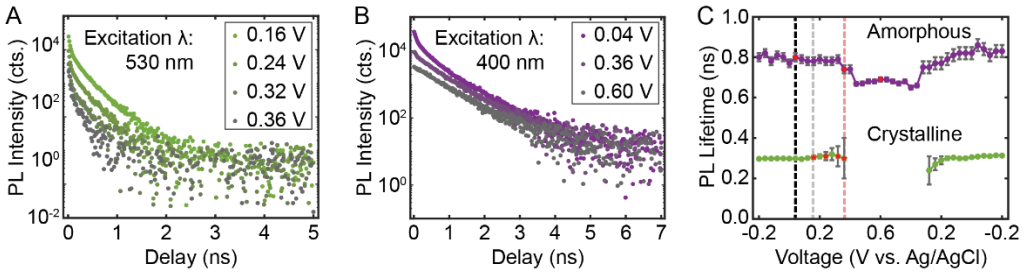

Figure 3. Voltage-dependent TRPL lifetimes of P3MEEET in 100 mM KCl. A) A series of TRPL traces using a 530 nm excitation source to probe changes in PL lifetime in crystalline regions with increased doping levels. B) TRPL traces using a 400 nm excitation source, showing corresponding changes in PL lifetime in amorphous regions. C) TRPL lifetimes for the amorphous and crystalline regions of P3MEEET as a function of applied voltage vs. Ag/AgCl. The red marks indicate where the representative TRPL traces lie on this plot. The black, gray, and red dotted lines correspond to the onset of PL intensity quenching from crystalline regions, the onset of PL intensity quenching from amorphous regions, and the onset of the PL lifetime decrease from amorphous regions, respectively.

Because both the amplitudes and lifetimes of the PL decay curves change with voltage, we fit the decay curves with exponential functions to extract amplitudes and lifetimes as a function of voltage. In the case of the 530 nm excitation, a sum of two exponential decay functions (**Equation 4**) was used to fit the decay trace plus a constant value to account for the dark counts (dark counts were determined by taking the average of the PL intensity counts after they decayed to the baseline, **Figure S6**):

$$I_A(t) = a_c e^{-\frac{t}{\tau_c}} + a_{IRF} e^{-\frac{t}{\tau_{IRF}}} + B \quad (4)$$

where *t* is the delay in nanoseconds, a_c is the amplitude of the crystalline component, a_{IRF} is the amplitude of the instrument response function (IRF), and *B* is the baseline. Further discussion of the origin of the IRF is included in the Supporting Information. The value for τ_{IRF} is 44.5 ± 0.7 ps, and τ_c is the PL lifetime due solely to emission from the crystalline regions of the polymer. The τ_c, a_c, and a_{IRF} values were determined using a least-squares regression of the voltage-dependent TRPL traces. The calculated values of a_c and a_{IRF} as a function of voltage vs. Ag/AgCl are depicted in **Figure S7**. The value of τ_{IRF} was calculated using a least-squares regression of the initial TRPL trace taken at -0.2 V—before any doping had occurred—and was kept constant from that point forward.

The value determined for τ_c from the measurement with an excitation wavelength of 530 nm was then used in a tri-exponential function (Equation 5) to fit the PL decay traces collected with 400 nm excitation:

$$I_B(t) = a_a e^{-\frac{t}{\tau_a}} + a_c e^{-\frac{t}{\tau_c}} + a_{IRF} e^{-\frac{t}{\tau_{IRF}}} + B \quad (5)$$

where *t* is the delay in nanoseconds, τ_a is the PL lifetime due to emission from the amorphous regions of the polymer, a_a is the amplitude of the exponential corresponding to the amorphous regions of the polymer, a_c is the amplitude of the exponential corresponding to the crystalline regions of the polymer, a_{IRF} is the amplitude of the IRF, and *B* is the baseline. The τ_a, a_a, a_c, and a_{IRF} values were then calculated using a least-squares regression, with a τ_{IRF} set at 57 ± 2 ps. The calculated values of a_a, a_c, and a_{IRF} as a function of voltage (vs. Ag/AgCl) are depicted in **Figure S8**. **Figure 3C** shows τ_a and τ_c as a function of voltage (vs. Ag/AgCl). A gap in the calculated values for τ_c is present because the PL signal from crystalline regions decays dramatically and becomes negligible at these doping levels. When there was no value to input for τ_c in Equation 5, a_c was assumed to be zero, essentially changing the triexponential function to a biexponential function similar to **Equation 4**.

When exciting the crystalline regions of P3MEEET, we find that the PL lifetime of P3MEEET remains constant at ~0.3 ns as we increase the voltage from -0.2 to 0.32 V (vs. Ag/AgCl). At 0.32 V, the PL signal decreases significantly, and we are no longer able to fit a PL decay (**Figure S8**). The amplitude of the PL decay curve recovers upon dedoping at 0.32 V and the PL lifetime again plateaus at ~0.3 ns. The PL lifetime of the amorphous regions plateaus at approximately 0.8 ns and then decreases at 0.32 V. The PL lifetime then recovers back to its original lifetime of approximately 0.8 ns at 0.32 V. The observed decrease in PL lifetime of the amorphous regions is not only caused by the large structural and electrochemical changes that alter chromophore properties as a result of inserting a substantial amount of ions into the polymer film, but also report on the properties of a subpopulation of chromophores that is not quenched. As mentioned earlier, this incomplete PL quenching of the amorphous regions may be due to low electronic mobility in those parts of the film.

In comparing the PL lifetimes and the steady-state PL intensities as a function of voltage, we find that the PL intensities are much more sensitive to electrochemical doping at low voltages than the PL lifetimes. Although significant quenching of the PL intensity occurs at relatively low voltages, we observe no change in the PL lifetime from the crystalline regions of the P3MEEET film. Furthermore, the change in lifetime of the amorphous regions of the P3MEEET film occurs 0.20 V higher than the onset of PL quenching of amorphous regions of the film.

To benchmark PL emission to other established methods that interrogate ion insertion in OMIECs, we perform four correlated *in situ* measurements as a function of voltage vs. Ag/AgCl. **Figure 4A** shows the integrated π-π* and polaron absorption intensities as a function of voltage from the UV-Vis spectroelectrochemistry spectra shown in **Figure 1**. We observe the characteristic reversible decrease in the π-π* absorption feature and an increase in the polaron feature. The ion density obtained through chronoamperometry follows a similar trend as the polaron absorption (**Figure 4B** and **Figure S9**) and the change in mass obtained with EQCM shows a slight initial decrease in mass followed by a large reversible increase (**Figure 4C** and

Figure S10). Last, by using *in situ* GIWAXS with a frit-based electrochemical cell (**Figure S11**),[55] we observe a reversible increase of the lamellar spacing as a function of voltage vs. Ag/AgCl (**Figure 4D** and **Figures S12-S13**). Overall, the initial changes in the π-π* and polaron absorption intensities, ion density, polymer mass, and lamellar spacing occur at approximately the same voltage of 0.2 V vs. Ag/AgCl.

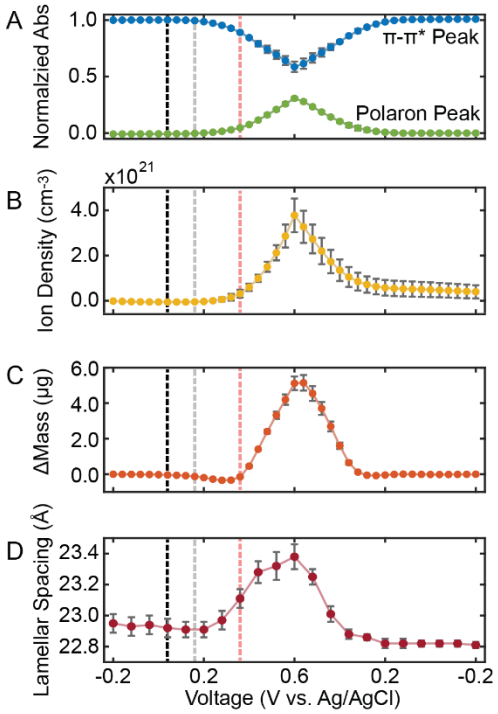

Figure 4. Correlated *in situ* methods for interrogating ion insertion in P3MEEET as a function of voltage. A) Integrated π-π* and polaron absorption. B) Ion density measured with chronoamperometry. C) Mass changes measured via EQCM. Each measurement was replicated on three different P3MEEET thin film samples with error bars representing a 95% confidence interval. D) Lamellar spacing of P3MEEET measured using in-situ GIWAXS. Error bars represent a 95% confidence interval of the Gaussian fit of the (300) peak corresponding to the lamellar spacing of P3MEEET. The black, gray, and red dotted lines correspond to the onset of PL quenching from crystalline regions, the onset of PL quenching from amorphous regions, and the onset of the PL lifetime decrease from amorphous regions, respectively.

By comparing changes in the four *in situ* methods in **Figure 4** to the changes in PL intensity and TRPL lifetime, we find that PL intensities are most sensitive to the onset of electrochemical doping. Specifically, quenching of the PL from crystalline and amorphous regions of P3MEEET occurs approximately 0.16 V and 0.04 V before changes in absorption, ion density, mass, and lamellar spacing. Yet, the change in the TRPL lifetime occurs at higher applied voltage than the *in situ* methods depicted in **Figure 4**. Overall, by comparing PL intensity and TRPL lifetimes to

other established methods that probe ion injection in OMIECs, we find that changes in PL intensity are most sensitive to electrochemical doping, while TRPL lifetimes are only sensitive to much higher doping levels.

To demonstrate that PL spectroelectrochemistry is a general tool for probing initial ion injection in crystalline and amorphous regions of OMIEC conjugated polymers, we acquired PL emission and absorption spectra as a function of voltage for two additional OMIECs, poly(3-[2-(2-methoxyethoxy)ethoxy]methylthiophene-2,5-diyl) (P3MEEMT) and poly(3-[4-carboxybutyl] thiophene-2,5-diyl) (P3CBT) (**Figure S14 A-B**). The PL spectra for P3MEEMT and P3CBT also quench as a function of voltage vs. Ag/AgCl (**Figure S14 C-F**). In comparing the PL emission and absorption spectroelectrochemistry measurements of both of these polymers, we find that PL emission is more sensitive to the initial steps of electrochemical doping compared to absorption spectroelectrochemistry. Furthermore, PL spectra of both P3MEEMT and P3CBT do not show the obvious separation of amorphous and crystalline regions present in P3MEEET. Therefore, rather than fitting each PL spectrum to crystalline and amorphous components, we integrate the high energy and low energy ends of the PL spectra and plot them as a function of voltage vs. Ag/AgCl (**Figure S14 G-H**). For both polymers, we find that quenching of the lower energy end of the PL spectrum occurs more steeply as a function of voltage than the higher energy ends of the spectra, indicating that ordered regions are doping before amorphous regions. We also find that ordered regions of these polymers dope more completely, while the disordered component still exhibits PL emission after the emission plateaus.

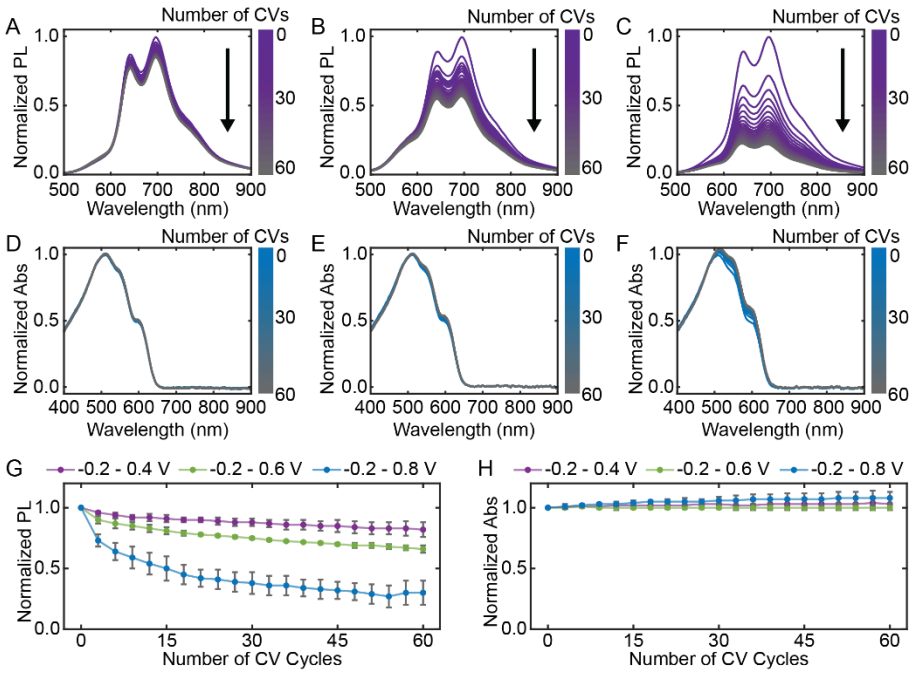

Figure 5. PL and absorption of P3MEEET upon CV cycling. A-C) PL spectra over 60 CV cycles over voltage windows of -0.2 to 0.4 V, -0.2 to 0.6 V, and -0.2 to 0.8 V, respectively. D-F) Corresponding changes in absorption under the same conditions. G) Normalized PL and H) normalized absorption as a function of the number of CV cycles.

Last, we show that PL spectroelectrochemistry is a sensitive probe of irreversible changes in the OMIEC upon repeated cycling. We performed 60 CVs of P3MEEET over three different voltage ranges, a low range (-0.2 V to 0.4 V), a medium range (-0.2 V to 0.6 V), and a high range (-0.2 V to 0.8 V), and collected a PL emission spectrum every 3 CVs upon dedoping. Examples of each of these CVs are depicted in **Figure S15**, which shows more significant changes occurring as the voltage range is increased. **Figures 5A-C** show examples of the series of PL spectra for each of the different voltage ranges. After 60 CV cycles were completed, the PL of the low-range CVs (-0.2 to 0.4 V) decreased on average by 18%, the mid-range (-0.2 to 0.6 V) by 34%, and the high-range (-0.2 to 0.8 V) by 70% (**Figure 5G**). We note that the decrease in PL emission intensity is not due to photobleaching, as each sample was exposed to the same flux regardless of voltage range and we observe a minimal decrease in PL emission intensity without performing CVs (**Figure S16**). We additionally collected absorption spectra over the same three voltage ranges (**Figures 5D-F**) and observed little change in the absorption for the low and mid-range voltages. However, for the high voltage range, the peak absorption intensity of P3MEEET slightly increased

in intensity by 8% (**Figure 5H**). These results demonstrate that changes in PL emission may be more sensitive than changes in absorption to degradation processes or structural transformations upon repeated doping cycles in OMIECs.

2. CONCLUSIONS

Our work establishes steady-state PL and TRPL spectroelectrochemistry as complementary techniques that probe photophysical changes in OMIECs in response to electrochemical doping. We find that steady-state PL spectroelectrochemistry can distinguish between electrochemical doping of amorphous and crystalline regions of OMIECs, serving as a sensitive indicator of the initial stages of electrochemical doping. In comparison, TRPL lifetimes remain largely constant at lower doping levels and only change past a relatively high doping threshold. Furthermore, steady-state PL intensity is much more sensitive to the initial intercalation of ions than other established *in situ* methods that probe ion injection in OMIECs. Steady-state PL emission intensity is also impacted by changes in the OMIEC upon repeated cycling, and these changes could serve as a sensitive indicator of degradation mechanisms that are not observed by other methods.

Additionally, compared to more complex *in situ* methods that probe ion intercalation, such as *in situ* GIWAXS and EQCM, acquiring steady-state PL spectra as a function of voltage is relatively straightforward, requiring only a potentiostat for applying a bias and a PL spectrometer for recording PL spectra. Overall, PL spectroelectrochemistry offers substantial insights into the photophysical properties of OMIECs during electrochemical doping. Because PL spectroelectrochemistry can differentiate between doping in disordered versus crystalline regions OMIECs, PL studies will aid in creating new design principles for the improvement of OMIEC-based devices, which may require a balance of disordered and ordered content.

3. EXPERIMENTAL SECTION

Materials Poly(3-[2-[2-(2-methoxyethoxy)ethoxy]ethyl]thiophene)-2,5-diyl (P3MEEET) was purchased from Rieke Metals (Lot BLS26-79, Mw = 12,000 g/mol, Pd = 1.6). Poly(3-[2-(2-methoxy ethoxy)ethoxy]methylthiophene-2,5-diyl) regioregular (P3MEEMT) was purchased from Rieke Metals (Lot PTL37-15, Mw = 23,000 g/mol, Pd = 2.1). Poly(3-[4-carboxybutyl]thiophene-2,5-diyl) (P3CBT) was purchased from Rieke Metals (Lot PTL42-45, Mw = 48,000 g/mol, Pd = 2.6). Potassium chloride (KCl) was purchased from Ward's Science. Isopropyl alcohol was purchased from VWR, acetone from Fisher Chemical, chlorobenzene from Sigma-Aldrich, chloroform from Fisher Chemical, and pyridine from Fisher Chemical.

Preparation of Polymer Solutions All solutions were prepared in an N_2 glovebox (LC Technology Solutions Inc.). P3MEEET and P3MEEMT were dissolved in anhydrous chlorobenzene in a 3 mL amber vial for a final 20 mg/mL concentration. P3CBT was dissolved in pyridine in a 3 mL amber vial for a final 20 mg/mL concentration. Polymer solutions were stirred for 24 hours at 60 ºC and filtered through a 0.2 µL syringe filter (Acrodisk) before processing.

Preparation of the KCl Aqueous Electrolyte The KCl aqueous electrolyte was prepared using 18.2 MΩ water (Millipore Milli-Q Advantage A10) and volumetric glassware to achieve a concentration of 100 mM. Before each electrochemistry experiment, the KCl electrolyte was degassed by bubbling N_2 for 10 minutes.

Preparation of Polymer Thin Films Glass coated with indium tin oxide (ITO) (MSE Supplies Inc.) was diced to 0.75 cm x 5 cm as substrates for spectroelectrochemistry measurements. The substrates were then cleaned in an ultrasonicator for 10 minutes each in a 1% Alconox aqueous solution (Alconox, Inc.), Milli-Q water, acetone, and isopropyl alcohol. The ITO glass substrates were dried with N_2 and placed in a plasma cleaner (Harrick Basic Plasma Cleaner) on high with ambient air for 10 minutes before spin-coating. A spin-coater (Ossila) was used to fabricate thin films on the ITO glass substrates. The polymer samples were prepared using 50 µL of solution

and spinning at 500 rpm for 5 seconds, then at 1000 rpm for 45 seconds. After spin-coating, the polymer thin films were annealed on a hotplate at 160 ºC for 7 minutes.

Absorption Spectroelectrochemistry Measurements Absorption spectroelectrochemistry measurements were performed using the Metrohm Autolab PGSTAT302N potentiostat and Autolab Spectrophotometer UV/Vis/NIR kit. The working electrode was an ITO-coated glass substrate, the reference electrode was an Ag/AgCl puck electrode (A-M Systems), and the counter electrode was a Pt mesh (Millipore Sigma). P3MEEET was equilibrated at -0.2 V for 30 seconds, followed by ten cyclic voltammetry cycles from -0.2 to 0.6 V at a scan rate of 0.1 $V*s^{-1}$ for each sample measurement. The sample was then equilibrated for 30 seconds, followed by a potentiostatic voltage ramp. The ramp used the specified range, with 0.04 V steps. Upon reaching the highest voltage of the specified range, the ramp was reversed back down to the initial voltage. Each step was held for 6 seconds, during which steady-state absorption measurements were collected with the NOVA 2.1.5 program, and the data was processed in MATLAB.[56]

Photoluminescence Spectroelectrochemistry Measurements Photoluminescence spectroelectrochemistry measurements were performed using the PalmSens4 potentiostat to control the electrochemical cell, the Ocean Optics QE65 Pro spectrometer for light detection, and a 405 nm LED (Thorlabs, M405L4) as the excitation source, using a 405 nm bandpass filter (Thorlabs) and a 450 nm long pass filter (Thorlabs) (**Figure S3**). The voltage ranges utilized for this experiment were -0.2 to 0.6 V for P3MEEET, -0.05 to 0.75 V for P3MEEMT, and -0.5 to 0.3 V for P3CBT. Samples were equilibrated at the lowest voltage of the selected range for 30 seconds, followed by ten cyclic voltammetry cycles using the polymer specific range at a scan rate of 0.1 $V*s^{-1}$ for each sample measurement. The sample was then equilibrated for 30 seconds, followed by a potentiostatic voltage ramp. The ramp used the specified range, with 0.04 V steps. Upon reaching the highest voltage of the specified range, the ramp was reversed back down to the initial voltage. Each step was held for 6 seconds, 1 second with the excitation source off and 5

seconds with the excitation on during the acquisition of the steady-state photoluminescence spectra. The PL spectrum of dilute P3MEEET dissolved in chloroform used the same apparatus, with an integration time of 5 seconds and no applied bias. Spectra were collected and processed in MATLAB.[56]

Time-Resolved Photoluminescence Measurements Time-resolved photoluminescence measurements were performed using a polarization-resolved epifluorescence setup described in our previous reports.[57] Briefly, the vertically polarized second harmonic of a pulsed Ti-sapphire laser (Coherent Chameleon Ultra II, repetition rate of 80 MHz) was used to excite the sample. Excitation wavelengths of 400 and 530 nm were used to selectively excite different chromophore populations in the semicrystalline polymer films. Excitation light was directed to the sample using a long-pass dichroic mirror—when the excitation was set to 400 nm, a dichroic with a 505 nm cutoff was employed (Thorlabs DMLP505R); when the excitation was set to 530 nm, a dichroic with a 562 nm cutoff was used (Thorlabs DMLP567). A 75 mm focal length lens was used to focus the excitation beam and collect the fluorescence emitted from the sample (epifluorescence configuration). On average, 90 μW power was used for the excitation beams at the sample position to avoid photodamaging the sample. When using 400 nm excitation, a 500 nm long-pass filter (Thorlabs FELH0500) was placed in the collection channel to reduce scattered/reflected light further. The fluorescence signal was split into horizontal and vertical polarization components with polarizing beam splitters and detected by matched single-photon avalanche detectors (Microphoton Devices (MPD)). The detector output was routed and recorded with a Time-Correlated Single Photon Counting (TCSPC) module (Picoquant PHR800 and Picoharp 300). Thin films of P3MEEET were placed in a 1 cm quartz cuvette with a 3D-printed sample holder to ensure consistent and stable sample positioning. The sample cell was loaded with ~3 mL of 100 mM KCl aqueous electrolyte solution—enough to cover the polymer film. Openings on the cuvette top were used to introduce reference (Ag/AgCl) and counter (Pt) electrodes; contact with the ITO

working electrode was made on the portion of the substrate not submerged in the electrolyte. Samples were first put through 10 CV cycles, ranging from -0.20 V to 0.60 V at a scan rate of 0.1 $V*s^{-1}$. The thin film was then electrochemically equilibrated for 20 seconds before recording signals, starting at -0.20 V, and going up in 0.04 V increments to 0.60 V, then reversing and going down to -0.20 V in the same increments. Integration times were optimized depending on the excitation conditions for each sample (100 seconds for 400 nm excitation and 50 seconds for 530 nm excitation of P3MEEET) and were kept constant throughout doping/dedoping cycles. All data sets were acquired with the instrument resolution set to 16 ps. Raw data was processed in MATLAB.[56] First, the average background signal (before the steep rise) was subtracted from the data, and the temporal axis was shifted to account for differences in the optical path and electronic delay of the signal from each polarization channel. Further, to match the signal collection efficiency of the two polarization channels, we inserted a factor (*g*) chosen so that the long-time asymptotic value of the transient fluorescence anisotropy decayed to zero (assuming complete depolarization in the amorphous channel).

EQCM Measurements EQCM measurements were performed using a Stanford QCM2000 5 MHz Quartz Crystal Microbalance and the Metrohm Autolab PGSTAT302N potentiostat. P3MEEET samples were equilibrated at -0.2 V for 30 seconds, followed by ten cyclic voltammetry cycles from -0.2 to 0.6 V at a scan rate of 0.1 $V*s^{-1}$ for each sample measurement. The sample was then equilibrated for 30 seconds, followed by a potentiostatic voltage ramp. The ramp ranged from -0.2 to 0.6 V, with 0.04 V steps that were held for 6 seconds. Upon reaching the highest voltage of the specified range, the ramp was reversed back down to the initial voltage. Voltage, frequency change, current, and charge as a function of time for the P3MEEET films were collected with the NOVA program. The resulting data was processed in MATLAB,[56] using the Sauerbrey equation to calculate mass changes from the measured changes in frequency.

Cyclic Voltammetry Cycling Spectroelectrochemistry Experiments Absorption and photoluminescence CV cycling spectroelectrochemistry experiments were performed using the same instrumental setup listed in the absorption and photoluminescence spectroelectrochemistry measurements. The sample of P3MEEET was equilibrated for this experiment at -0.5 V for 30 seconds, and then an initial absorption spectrum was taken. Then, 60 CVs were run on the sample, with voltage ranges of -0.2 to 0.4 V, -0.2 to 0.6 V, and -0.2 to 0.8 V at a scan rate of 0.1 $V*s^{-1}$. Every three CV cycles, the sample was again equilibrated at -0.5 V for 30 seconds before a spectrum was taken. CVs, absorption, and PL data were processed in MATLAB.[56]

GIWAXS Measurements *In situ* GIWAXS measurements were collected at the Advanced Light source (ALS) at the Lawrence Berkeley National Labs on beamline 7.3.3.[58] A frit cell, composed of Au-coated silicon porous chip and a 3D printed structure, was devised to measure the lamellar spacing of P3MEEET *in situ* (**Figure S10**). P3MEEET was first spin coated onto a glass slide, then floated off of the glass slide into Milli-Q water before being lifted onto the Au-coated silicon chip. After putting the sample into the helium chamber, P3MEEET samples were equilibrated at -0.2 V for 30 seconds, followed by ten cyclic voltammetry cycles from -0.2 to 0.6 V at a scan rate of 0.1 $V*s^{-1}$ for each sample measurement. The sample was then equilibrated for 30 seconds, followed by a potentiostatic voltage ramp. The ramp ranged from -0.2 to 0.6 V, with 0.08 V steps that were equilibrated for 10 seconds before taking a measurement, followed by an X-ray exposure time of 5 seconds. Upon reaching the highest voltage of the specified range, the ramp was reversed back down to the initial voltage. All diffraction images and data reductions were processed in Igor Pro using the Nika and WAXSTools software packages,[59,60] followed by further processing in MATLAB.[56]

UV-Vis-NIR Measurements UV-Vis-NIR measurements were performed on Perkin Elmer Lambda 950 UV-Vis-NIR with a wavelength range of 300 to 1000 nm, scan rate of 2 $nm*s^{-1}$, and a slit size of 2 nm. The thin films were prepared by spin coating 50 µL of P3MEEET on a 0.75 x 5

cm quartz substrate (Ted Pella) at a rate of 500 rpm for 5 seconds, then 1000 rpm for 45 seconds. A blank quartz substrate was used as a background. Absorbance measurements were processed in MATLAB.[56]

AFM Measurements Topography and thickness measurements were collected using a Molecular Vista One Atomic Force Microscope (AFM) and Pt/Ir Tip (Molecular Vista). The P3MEEET thin films were prepared using the same method for spectroelectrochemical measurements. Topography images were acquired using a scan rate of 0.1 lines*s^{-1} and an image size of 256 x 256 pixels and 10 μm x 10 μm. Surface roughness was calculated by taking the root mean square of the AFM image. The thickness of P3MEEET thin films were determined by scratching the thin film and measuring the average height difference between the film and the substrate. All images were processed in SurfaceWorks software (Molecular Vista) and MATLAB.[56]

ACKNOWLEDGEMENTS

This work was supported by the National Science Foundation (CHE-2304613). G.W.C. and C.G.B. acknowledge partial financial support from MathWorks for data analysis. Beamline 7.3.3 of the Advanced Light Source is supported by the Director of the Office of Science, Office of Basic Energy Sciences, of the U.S. Department of Energy under Contract No. DE-AC02-05CH11231. UV-Vis-NIR measurements were performed at the University of Utah's Materials Characterization Lab. G.W.C., S.R.J., J.N.K., and R.L.K. thank Bryan Paulsen, Chenhui Zhu, and Eric Schaible for helpful discussions and instrument support.

REFERENCES

(1) Paulsen, B. D.; Tybrandt, K.; Stavrinidou, E.; Rivnay, J. Organic Mixed Ionic–Electronic Conductors. *Nat. Mater.* **2020**, *19* (1), 13–26. https://doi.org/10.1038/s41563-019-0435-z.
(2) Inal, S.; Rivnay, J.; Suiu, A.-O.; Malliaras, G. G.; McCulloch, I. Conjugated Polymers in Bioelectronics. *Acc. Chem. Res.* **2018**, *51* (6), 1368–1376. https://doi.org/10.1021/acs.accounts.7b00624.
(3) Rivnay, J.; Owens, R. M.; Malliaras, G. G. The Rise of Organic Bioelectronics. *Chem. Mater.* **2014**, *26* (1), 679–685. https://doi.org/10.1021/cm4022003.

(4) Keene, S. T.; Fogarty, D.; Cooke, R.; Casadevall, C. D.; Salleo, A.; Parlak, O. Wearable Organic Electrochemical Transistor Patch for Multiplexed Sensing of Calcium and Ammonium Ions from Human Perspiration. *Adv. Healthc. Mater.* **2019**, *8* (24), 1901321. https://doi.org/10.1002/adhm.201901321.
(5) Liu, Q.; Liu, Y.; Li, J.; Lau, C.; Wu, F.; Zhang, A.; Li, Z.; Chen, M.; Fu, H.; Draper, J.; Cao, X.; Zhou, C. Fully Printed All-Solid-State Organic Flexible Artificial Synapse for Neuromorphic Computing. *ACS Appl. Mater. Interfaces* **2019**, *11* (18), 16749–16757. https://doi.org/10.1021/acsami.9b00226.
(6) Harikesh, P. C.; Yang, C.-Y.; Wu, H.-Y.; Zhang, S.; Donahue, M. J.; Caravaca, A. S.; Huang, J.-D.; Olofsson, P. S.; Berggren, M.; Tu, D.; Fabiano, S. Ion-Tunable Antiambipolarity in Mixed Ion–Electron Conducting Polymers Enables Biorealistic Organic Electrochemical Neurons. *Nat. Mater.* **2023**, *22* (2), 242–248. https://doi.org/10.1038/s41563-022-01450-8.
(7) van de Burgt, Y.; Lubberman, E.; Fuller, E. J.; Keene, S. T.; Faria, G. C.; Agarwal, S.; Marinella, M. J.; Alec Talin, A.; Salleo, A. A Non-Volatile Organic Electrochemical Device as a Low-Voltage Artificial Synapse for Neuromorphic Computing. *Nat. Mater.* **2017**, *16* (4), 414–418. https://doi.org/10.1038/nmat4856.
(8) *Organic Electrode Materials for Rechargeable Lithium Batteries - Liang - 2012 - Advanced Energy Materials - Wiley Online Library*. https://onlinelibrary-wiley-com.ezproxy.lib.utah.edu/doi/full/10.1002/aenm.201100795 (accessed 2023-12-04).
(9) Snook, G. A.; Kao, P.; Best, A. S. Conducting-Polymer-Based Supercapacitor Devices and Electrodes. *J. Power Sources* **2011**, *196* (1), 1–12. https://doi.org/10.1016/j.jpowsour.2010.06.084.
(10) Wu, R.; Matta, M.; Paulsen, B. D.; Rivnay, J. Operando Characterization of Organic Mixed Ionic/Electronic Conducting Materials. *Chem. Rev.* **2022**, *122* (4), 4493–4551. https://doi.org/10.1021/acs.chemrev.1c00597.
(11)Ohayon, D.; Druet, V.; Inal, S. A Guide for the Characterization of Organic Electrochemical Transistors and Channel Materials. *Chem. Soc. Rev.* **2023**, *52* (3), 1001–1023. https://doi.org/10.1039/D2CS00920J.
(12) Giovannitti, A.; Sbircea, D.-T.; Inal, S.; Nielsen, C. B.; Bandiello, E.; Hanifi, D. A.; Sessolo, M.; Malliaras, G. G.; McCulloch, I.; Rivnay, J. Controlling the Mode of Operation of Organic Transistors through Side-Chain Engineering. *Proc. Natl. Acad. Sci.* **2016**, *113* (43), 12017–12022. https://doi.org/10.1073/pnas.1608780113.
(13) Garreau, S.; Louarn, G.; Buisson, J. P.; Froyer, G.; Lefrant, S. In Situ Spectroelectrochemical Raman Studies of Poly(3,4-Ethylenedioxythiophene) (PEDT). *Macromolecules* **1999**, *32* (20), 6807–6812. https://doi.org/10.1021/ma9905674.
(14) Eng, M. P.; Barnes, P. R. F.; Durrant, J. R. Concentration-Dependent Hole Mobility and Recombination Coefficient in Bulk Heterojunctions Determined from Transient Absorption Spectroscopy. *J. Phys. Chem. Lett.* **2010**, *1* (20), 3096–3100. https://doi.org/10.1021/jz1011803.
(15) Cavassin, P.; Holzer, I.; Tsokkou, D.; Bardagot, O.; Réhault, J.; Banerji, N. Electrochemical Doping in Ordered and Disordered Domains of Organic Mixed Ionic–Electronic Conductors. *Adv. Mater.* **2023**, *35* (35), 2300308. https://doi.org/10.1002/adma.202300308.
(16) Takahara, A.; Higaki, Y.; Hirai, T.; Ishige, R. Application of Synchrotron Radiation X-Ray Scattering and Spectroscopy to Soft Matter. *Polymers* **2020**, *12* (7), 1624. https://doi.org/10.3390/polym12071624.
(17) Aime, J. P.; Bargain, F.; Schott, M.; Eckhardt, H.; Miller, G. G.; Elsenbaumer, R. L. Structural Study of Doped and Undoped Polythiophene in Solution by Small-Angle Neutron Scattering. *Phys. Rev. Lett.* **1989**, *62* (1), 55–58. https://doi.org/10.1103/PhysRevLett.62.55.
(18) Du, W.; Ohayon, D.; Combe, C.; Mottier, L.; Maria, I. P.; Ashraf, R. S.; Fiumelli, H.; Inal, S.; McCulloch, I. Improving the Compatibility of Diketopyrrolopyrrole Semiconducting

Polymers for Biological Interfacing by Lysine Attachment. *Chem. Mater.* **2018**, *30* (17), 6164–6172. https://doi.org/10.1021/acs.chemmater.8b02804.
(19) Lyu, D.; Jin, Y.; Magusin, P. C. M. M.; Sturniolo, S.; Zhao, E. W.; Yamamoto, S.; Keene, S. T.; Malliaras, G. G.; Grey, C. P. Operando NMR Electrochemical Gating Studies of Ion Dynamics in PEDOT:PSS. *Nat. Mater.* **2023**, *22* (6), 746–753. https://doi.org/10.1038/s41563-023-01524-1.
(20) Zozoulenko, I.; Singh, A.; Singh, S. K.; Gueskine, V.; Crispin, X.; Berggren, M. Polarons, Bipolarons, And Absorption Spectroscopy of PEDOT. *ACS Appl. Polym. Mater.* **2019**, *1* (1), 83–94. https://doi.org/10.1021/acsapm.8b00061.
(21) Bischak, C. G.; Flagg, L. Q.; Yan, K.; Rehman, T.; Davies, D. W.; Quezada, R. J.; Onorato, J. W.; Luscombe, C. K.; Diao, Y.; Li, C.-Z.; Ginger, D. S. A Reversible Structural Phase Transition by Electrochemically-Driven Ion Injection into a Conjugated Polymer. *J. Am. Chem. Soc.* **2020**, *142* (16), 7434–7442. https://doi.org/10.1021/jacs.9b12769.
(22) Giridharagopal, R.; Flagg, L. Q.; Harrison, J. S.; Ziffer, M. E.; Onorato, J.; Luscombe, C. K.; Ginger, D. S. Electrochemical Strain Microscopy Probes Morphology-Induced Variations in Ion Uptake and Performance in Organic Electrochemical Transistors. *Nat. Mater.* **2017**, *16* (7), 737–742. https://doi.org/10.1038/nmat4918.
(23) Collins, S. D.; Mikhnenko, O. V.; Nguyen, T. L.; Rengert, Z. D.; Bazan, G. C.; Woo, H. Y.; Nguyen, T.-Q. Observing Ion Motion in Conjugated Polyelectrolytes with Kelvin Probe Force Microscopy. *Adv. Electron. Mater.* **2017**, *3* (3), 1700005. https://doi.org/10.1002/aelm.201700005.
(24) Skompska, M.; Szkurlat, A.; Kowal, A.; Szklarczyk, M. Spectroelectrochemical and AFM Studies of Doping−Undoping of Poly(3-Hexylthiophene) Films in Propylene Carbonate and Aqueous Solutions of LiClO4. *Langmuir* **2003**, *19* (6), 2318–2324. https://doi.org/10.1021/la0261850.
(25) Moser, M.; Savva, A.; Thorley, K.; Paulsen, B. D.; Hidalgo, T. C.; Ohayon, D.; Chen, H.; Giovannitti, A.; Marks, A.; Gasparini, N.; Wadsworth, A.; Rivnay, J.; Inal, S.; McCulloch, I. Polaron Delocalization in Donor–Acceptor Polymers and Its Impact on Organic Electrochemical Transistor Performance. *Angew. Chem. Int. Ed.* **2021**, *60* (14), 7777–7785. https://doi.org/10.1002/anie.202014078.
(26) Parr, Z. S.; Rashid, R. B.; Paulsen, B. D.; Poggi, B.; Tan, E.; Freeley, M.; Palma, M.; Abrahams, I.; Rivnay, J.; Nielsen, C. B. Semiconducting Small Molecules as Active Materials for p-Type Accumulation Mode Organic Electrochemical Transistors. *Adv. Electron. Mater.* **2020**, *6* (6), 2000215. https://doi.org/10.1002/aelm.202000215.
(27) Yamamoto, J.; Furukawa, Y. Raman Characterization and Electrical Properties of Poly(3-Hexylthiophene) Doped Electrochemically in an Ionic Liquid-Gated Transistor Geometry. *Org. Electron.* **2016**, *28*, 82–87. https://doi.org/10.1016/j.orgel.2015.10.016.
(28) Wood, S.; Hollis, J. R.; Kim, J.-S. Raman Spectroscopy as an Advanced Structural Nanoprobe for Conjugated Molecular Semiconductors. *J. Phys. Appl. Phys.* **2017**, *50* (7), 073001. https://doi.org/10.1088/1361-6463/50/7/073001.
(29) Enokida, I.; Furukawa, Y. Doping-Level Dependent Mobilities of Positive Polarons and Bipolarons in Poly(2,5-Bis(3-Hexadecylthiophen-2-Yl)Thieno[3,2-b]Thiophene) (PBTTT-C16) Based on an Ionic-Liquid-Gated Transistor Configuration. *Org. Electron.* **2019**, *68*, 28–34. https://doi.org/10.1016/j.orgel.2019.01.045.
(30) Knowles, K. E.; Koch, M. D.; Shelton, J. L. Three Applications of Ultrafast Transient Absorption Spectroscopy of Semiconductor Thin Films: Spectroelectrochemistry, Microscopy, and Identification of Thermal Contributions. *J. Mater. Chem. C* **2018**, *6* (44), 11853–11867. https://doi.org/10.1039/C8TC02977F.
(31) Tsokkou, D.; Peterhans, L.; Cao, D. X.; Mai, C.-K.; Bazan, G. C.; Nguyen, T.-Q.; Banerji, N. Excited State Dynamics of a Self-Doped Conjugated Polyelectrolyte. *Adv. Funct. Mater.* **2020**, *30* (9), 1906148. https://doi.org/10.1002/adfm.201906148.

(32) Bargigia, I.; Savagian, L. R.; Österholm, A. M.; Reynolds, J. R.; Silva, C. Charge-Transfer Intermediates in the Electrochemical Doping Mechanism of Conjugated Polymers. *J. Am. Chem. Soc.* **2021**, *143* (1), 294–308. https://doi.org/10.1021/jacs.0c10692.
(33) Coropceanu, V.; Cornil, J.; da Silva Filho, D. A.; Olivier, Y.; Silbey, R.; Brédas, J.-L. Charge Transport in Organic Semiconductors. *Chem. Rev.* **2007**, *107* (4), 926–952. https://doi.org/10.1021/cr050140x.
(34) Liu, C.; Huang, K.; Park, W.-T.; Li, M.; Yang, T.; Liu, X.; Liang, L.; Minari, T.; Noh, Y.-Y. A Unified Understanding of Charge Transport in Organic Semiconductors: The Importance of Attenuated Delocalization for the Carriers. *Mater. Horiz.* **2017**, *4* (4), 608–618. https://doi.org/10.1039/C7MH00091J.

(35) Dyreklev, P.; Inganäs, O.; Paloheimo, J.; Stubb, H. Photoluminescence Quenching in a Polymer Thin-film Field-effect Luministor. *J. Appl. Phys.* **1992**, *71* (6), 2816–2820. https://doi.org/10.1063/1.351010.
(36) van Reenen, S.; Vitorino, M. V.; Meskers, S. C. J.; Janssen, R. A. J.; Kemerink, M. Photoluminescence Quenching in Films of Conjugated Polymers by Electrochemical Doping. *Phys. Rev. B* **2014**, *89* (20), 205206. https://doi.org/10.1103/PhysRevB.89.205206.
(37) Park, S.-J.; Gesquiere, A. J.; Yu, J.; Barbara, P. F. Charge Injection and Photooxidation of Single Conjugated Polymer Molecules. *J. Am. Chem. Soc.* **2004**, *126* (13), 4116–4117. https://doi.org/10.1021/ja031929x.
(38) Hayashi, S.; Kaneto, K.; Yoshino, K. Quenching of Photoluminescence in Poly(Thiophene) Films by Electrochemical Doping. *Solid State Commun.* **1987**, *61* (4), 249–251. https://doi.org/10.1016/0038-1098(87)91012-X.
(39) Edman, L.; Summers, M. A.; Buratto, S. K.; Heeger, A. J. Polymer Light-Emitting Electrochemical Cells: Doping, Luminescence, and Mobility. *Phys. Rev. B* **2004**, *70* (11), 115212. https://doi.org/10.1103/PhysRevB.70.115212.
(40) Meier, S. B.; Hartmann, D.; Tordera, D.; Bolink, H. J.; Winnacker, A.; Sarfert, W. Dynamic Doping and Degradation in Sandwich-Type Light-Emitting Electrochemical Cells. *Phys. Chem. Chem. Phys.* **2012**, *14* (31), 10886–10890. https://doi.org/10.1039/C2CP41323J.
(41) Holt, A. L.; Leger, J. M.; Carter, S. A. Electrochemical and Optical Characterization of P- and n-Doped Poly[2-Methoxy-5-(2-Ethylhexyloxy)-1,4-Phenylenevinylene]. *J. Chem. Phys.* **2005**, *123* (4), 044704. https://doi.org/10.1063/1.1949188.
(42) Gao, J.; Dane, J. Visualization of Electrochemical Doping and Light-Emitting Junction Formation in Conjugated Polymer Films. *Appl. Phys. Lett.* **2004**, *84* (15), 2778–2780. https://doi.org/10.1063/1.1702126.
(43) Hu, Y.; Tracy, C.; Gao, J. High-Resolution Imaging of Electrochemical Doping and Dedoping Processes in Luminescent Conjugated Polymers. *Appl. Phys. Lett.* **2006**, *88* (12), 123507. https://doi.org/10.1063/1.2187408.
(44) Sim, M.; Shin, J.; Shim, C.; Kim, M.; Jo, S. B.; Kim, J.-H.; Cho, K. Dependence of Exciton Diffusion Length on Crystalline Order in Conjugated Polymers. *J. Phys. Chem. C* **2014**, *118* (2), 760–766. https://doi.org/10.1021/jp409776s.
(45) Rörich, I.; Mikhnenko, O. V.; Gehrig, D.; Blom, P. W. M.; Crăciun, N. I. Influence of Energetic Disorder on Exciton Lifetime and Photoluminescence Efficiency in Conjugated Polymers. *J. Phys. Chem. B* **2017**, *121* (6), 1405–1412. https://doi.org/10.1021/acs.jpcb.6b11813.
(46) Spano, F. C.; Silva, C. H- and J-Aggregate Behavior in Polymeric Semiconductors. *Annu. Rev. Phys. Chem.* **2014**, *65*, 477–500. https://doi.org/10.1146/annurev-physchem-040513-103639.
(47) Clark, J.; Silva, C.; Friend, R. H.; Spano, F. C. Role of Intermolecular Coupling in the Photophysics of Disordered Organic Semiconductors: Aggregate Emission in Regioregular

Polythiophene. *Phys. Rev. Lett.* **2007**, *98* (20), 206406. https://doi.org/10.1103/PhysRevLett.98.206406.
(48) Thomas, E. M.; Brady, M. A.; Nakayama, H.; Popere, B. C.; Segalman, R. A.; Chabinyc, M. L. X-Ray Scattering Reveals Ion-Induced Microstructural Changes During Electrochemical Gating of Poly(3-Hexylthiophene). *Adv. Funct. Mater.* **2018**, *28* (44), 1803687. https://doi.org/10.1002/adfm.201803687.
(49) Jackson, S. R.; Kingsford, R. L.; Collins, G. W.; Bischak, C. G. Crystallinity Determines Ion Injection Kinetics and Local Ion Density in Organic Mixed Conductors. *Chem. Mater.* **2023**, *35* (14), 5392–5400. https://doi.org/10.1021/acs.chemmater.3c00657.
(50) Schmode, P.; Savva, A.; Kahl, R.; Ohayon, D.; Meichsner, F.; Dolynchuk, O.; Thurn-Albrecht, T.; Inal, S.; Thelakkat, M. The Key Role of Side Chain Linkage in Structure Formation and Mixed Conduction of Ethylene Glycol Substituted Polythiophenes. *ACS Appl. Mater. Interfaces* **2020**, *12* (11), 13029–13039. https://doi.org/10.1021/acsami.9b21604.
(51) Tropp, J.; Meli, D.; Wu, R.; Xu, B.; Hunt, S. B.; Azoulay, J. D.; Paulsen, B. D.; Rivnay, J. Revealing the Impact of Molecular Weight on Mixed Conduction in Glycolated Polythiophenes through Electrolyte Choice. *ACS Mater. Lett.* **2023**, *5* (5), 1367–1375. https://doi.org/10.1021/acsmaterialslett.2c01114.
(52) Rivnay, J.; Mannsfeld, S. C. B.; Miller, C. E.; Salleo, A.; Toney, M. F. Quantitative Determination of Organic Semiconductor Microstructure from the Molecular to Device Scale. *Chem. Rev.* **2012**, *112* (10), 5488–5519. https://doi.org/10.1021/cr3001109.
(53) Yee, P. Y.; Scholes, D. T.; Schwartz, B. J.; Tolbert, S. H. Dopant-Induced Ordering of Amorphous Regions in Regiorandom P3HT. *J. Phys. Chem. Lett.* **2019**, *10* (17), 4929–4934. https://doi.org/10.1021/acs.jpclett.9b02070.
(54) Mele, E.; Lezzi, F.; Polini, A.; Altamura, D.; Giannini, C.; Pisignano, D. Enhanced Charge-Carrier Mobility in Polymer Nanofibers Realized by Solvent-Resistant Soft Nanolithography. *J. Mater. Chem.* **2012**, *22* (34), 18051–18056. https://doi.org/10.1039/C2JM33611A.
(55) Paulsen, B. D.; Giovannitti, A.; Wu, R.; Strzalka, J.; Zhang, Q.; Rivnay, J.; Takacs, C. J. Electrochemistry of Thin Films with In Situ/Operando Grazing Incidence X-Ray Scattering: Bypassing Electrolyte Scattering for High Fidelity Time Resolved Studies. *Small* **2021**, *17* (42), 2103213. https://doi.org/10.1002/smll.202103213.
(56) The Mathworks Inc. MATLAB, 2022. https://www.mathworks.com.
(57) Singh, R. K.; Jonely, M.; Leslie, E.; Rejali, N. A.; Noriega, R.; Bass, B. L. Transient Kinetic Studies of the Antiviral Drosophila Dicer-2 Reveal Roles of ATP in Self-Nonself Discrimination. *eLife* **2021**, *10*, e65810. https://doi.org/10.7554/eLife.65810.
(58) Hexemer, A.; Bras, W.; Glossinger, J.; Schaible, E.; Gann, E.; Kirian, R.; MacDowell, A.; Church, M.; Rude, B.; Padmore, H. A SAXS/WAXS/GISAXS Beamline with Multilayer Monochromator. *J. Phys. Conf. Ser.* **2010**, *247* (1), 012007. https://doi.org/10.1088/1742-6596/247/1/012007.
(59) Ilavsky, J. Nika: Software for Two-Dimensional Data Reduction. *J. Appl. Crystallogr.* **2012**, *45* (2), 324–328. https://doi.org/10.1107/S0021889812004037.
(60) Zhang, F.; Ilavsky, J.; Long, G. G.; Quintana, J. P. G.; Allen, A. J.; Jemian, P. R. Glassy Carbon as an Absolute Intensity Calibration Standard for Small-Angle Scattering. *Metall. Mater. Trans. A* **2010**, *41* (5), 1151–1158. https://doi.org/10.1007/s11661-009-9950-x.